Long-Lived Mechanically Detected Molecular Spins for Quantum Sensing

Sahand Tabatabaei, Pritam Priyadarsi, Daniel Tay, Namanish Singh, Pardis Sahafi, Andrew Jordan, and Raffi Budakian*

Department of Physics and Astronomy, University of Waterloo, Waterloo, Ontario, Canada, N2L3G1 and Institute for Quantum Computing, University of Waterloo, Waterloo, Ontario, Canada, N2L3G1

(Received 6 March 2026; revised 18 May 2026; accepted 1 June 2026; published 27 July 2026)

Quantum sensors based on individual spins provide unprecedented access to local magnetic fields in condensed matter, chemistry, and biology, with solid-state defect spins emerging as the leading platform. However, their molecular-sensing capabilities are limited by confinement to a host lattice, which prevents placement in close proximity to a target molecule. Molecular spins offer an alternative, enabling chemical tunability and flexible positioning relative to the target system. Here we present a nanoscale sensing platform that combines molecular electron spins, ultrasensitive mechanical readout, and Hamiltonian engineering. Using a modified XYXY dipolar decoupling sequence, we suppress electron-electron dipolar interactions across a broad distribution of control fields, extending coherence times to ∼400 μs in an attoliter-scale droplet containing ∼100 trityl-OX063 radicals. Leveraging this sequence, we demonstrate frequency-selective detection of nanotesla-scale ac fields and perform sensing and spectroscopy of small, local nuclear-spin ensembles. Collectively, these results establish spin-based quantum integrated nanomechanical transduction as a framework for quantum sensing that affords molecular-level control over sensor properties and enables direct integration into complex molecular targets.

DOI: 10.1103/c994-bzx7

Subject Areas: Condensed Matter Physics, Quantum Physics

I. INTRODUCTION

The ability to control and detect nuclear and electron spins via magnetic resonance has fundamentally transformed our understanding of molecular structure, condensed matter systems, and chemistry, forming the bedrock of powerful techniques such as magnetic resonance imaging and spectroscopy. Building on this foundation, developments in quantum technologies have reimagined individual spins as nanoscale probes of their environment, capable of detecting magnetic fields [1–3], temperature [4,5], and strain [6,7] with exceptional sensitivity. Such quantum sensors have been proposed for extracting molecular-scale structural information from biomolecules and complex materials [8–12], imaging quasiparticle excitations in condensed matter [13–15], probing chemical processes [16–18], and even searching for physics beyond the standard model [19–21].

Among existing platforms, nitrogen-vacancy (NV) centers in diamond [9,22,23] are a leading candidate, offering optical initialization and readout with long coherence times under ambient conditions. These features have enabled landmark experiments ranging from magnetic resonance spectroscopy of single proteins [10] to atomic-resolution imaging of nuclear spins within the diamond [24,25]. Nonetheless, bringing the NV sensor close to the target is challenging, as shallow NV centers often have unstable charge states under optical illumination [26], along with reduced coherence times due to magnetic and electric field noise near the diamond surface [27–29]. Despite ongoing efforts to mitigate these effects [26,30–32], achieving robust NV operation within a few nanometers of the surface remains a persistent challenge, motivating alternative platforms such as defects in two-dimensional materials [33–35]. More generally, defect-based sensors are inherently constrained by their host crystals, limiting how sensor spins can be positioned or oriented relative to a target. This has prompted interest in molecular spin systems as alternative quantum sensors whose placement and spin properties can be chemically engineered [36–38].

Molecular radicals are a particularly well-established class of spin systems that have long served as versatile probes in electron spin resonance (ESR) spectroscopy [39–41]. Decades of ESR research have yielded a comprehensive understanding of their spin dynamics, along with mature techniques for chemically synthesizing, functionalizing, and positioning radicals within a few

*Contact author: rbudakian@uwaterloo.ca

Published by the American Physical Society under the terms of the Creative Commons Attribution 4.0 International license. Further distribution of this work must maintain attribution to the author(s) and the published article's title, journal citation, and DOI.

nanometers of target molecules, either through site-directed attachment or by embedding them within the material under study [42–45]. These capabilities provide a degree of chemical tunability unique to molecular spin systems [36]. In addition, established cryoprotectants from structural biology enable low-temperature operation of the radicals while preserving the sample's structural integrity [46]. These features suggest that molecular radicals can serve as sensor spins placed in close and flexible arrangements relative to a target sample to interrogate its local magnetic environment. However, their potential as quantum sensors has heretofore remained largely unexplored, in part because their coherence times are typically short—often less than ∼10 μs depending on the radical and its environment, even at low temperatures [47–50]. Furthermore, although optically addressable molecular spin systems are being developed [36,51–54], many existing ESR radicals—including nitroxides and trityls, the workhorses of modern structural biology—lack optical addressability. This limitation motivates alternative approaches that can harness these established radicals for quantum sensing and potentially transform structural biology.

In this work, we introduce SQUINT (spin-based quantum integrated nanomechanical transduction), a nanoscale quantum-sensing platform that integrates molecular electron spins with ultrasensitive mechanical readout and Hamiltonian engineering. SQUINT builds on experimental infrastructure developed for force-detected nanoscale magnetic resonance imaging (nanoMRI) [9], enabling high-fidelity control and detection of nanoscale electron-spin ensembles while providing access to large, time-dependent magnetic-field gradients for high-resolution spatial encoding [55–57].

We use the electron spin in trityl-OX063 radicals as the quantum sensor. To preserve coherence in these ensembles, we introduce a modified XYXY dipolar decoupling (XYXYd) sequence that suppresses electron-electron interactions, extending coherence times up to ∼400 μs. Using this sequence, we demonstrate frequency-selective sensing of nanotesla-scale ac magnetic fields, and perform nuclear-spin sensing and spectroscopy of ^{1}H and 1% natural-abundance ^{13}C spins on the OX063 molecule. Sensitivity analysis indicates that near-term improvements to the mechanical readout could enable detection of individual ^{1}H spins using a single electron spin at nanoscale separations. Together, these results establish a route to leveraging widely used molecular radicals as practical quantum sensors for probing local magnetic environments in molecular systems.

II. SENSING PLATFORM

A. OX063 molecular quantum sensor

Each trityl-OX063 molecule [Fig. 1(c)] is a stable organic radical with a single unpaired electron primarily localized on the central carbon of the trityl core. In a static magnetic field, this spin ($S = 1/2$) defines a coherently addressable two-level system and serves as the quantum sensor in SQUINT. During a sensing sequence, variations in the local magnetic field modulate the electron-spin Zeeman splitting, producing phase accumulation of the spin coherence that is subsequently mapped onto longitudinal magnetization and read out mechanically.

In OX063, the unpaired electron is sterically shielded by three sulfur-substituted phenyl rings. The shielding limits close contact between the radical center and surrounding

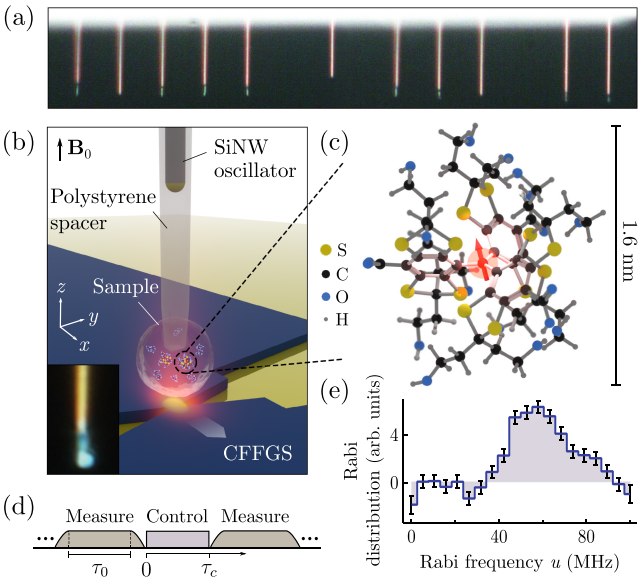


FIG. 1. SQUINT sensing platform. (a) Optical image of the SiNW chip, showing an array of SiNW mechanical sensors fabricated along the chip edge. (b) Schematic of the sensing platform, including the SiNW oscillator, sample, polystyrene spacer, and current-focusing field gradient source (CFFGS). The bright red region indicates the spatial profile of the readout gradient. The molecules depicted inside the sample droplet are trehalose and trityl-OX063. Inset: enlarged optical image of the tip of a SiNW, showing the polystyrene spacer and attached sugar droplet. (c) Molecular structure of the trityl-OX063 radical, with the central unpaired electron (red arrow) serving as the sensor spin. (d) Schematic of the correlation-based spin measurement protocol. The signal is obtained by correlating the readout-gradient-weighted longitudinal magnetization measured before and after a control sequence of duration τ_c, with repeated measurement windows of duration τ_0. Each measure block is composed of the MAGGIC spin detection sequence [55–57]. (e) Distribution of electron Rabi frequencies for the sample used in this work. The distribution was measured by driving the electron spins at the electron Larmor frequency with microwave pulses of variable encoding duration, following the Fourier encoding scheme described in Refs. [56,57]. Each spin accumulates a rotation set by its local Rabi frequency, and a Fourier cosine transform of the measured signal gives the distribution of u weighted by the readout gradient squared. The Rabi frequencies shown correspond to a peak current of 5 mA through the CFFGS.

spins, reducing unwanted magnetic interactions while preserving magnetic coupling to the local environment [47,58]. Together with the high molecular symmetry of the radical, this protection gives OX063 a narrow ESR spectrum and small g anisotropy compared with many other organic radicals [58]. The peripheral carboxyl and hydroxyl groups improve water solubility and biocompatibility, and allow OX063 to be used in aqueous and glassy sugar cryoprotectant matrices [45,59].

Functionalized OX063 derivatives also provide chemical handles for site-directed labeling of proteins and other target molecules [44,45]. Taken together, these features make OX063 and related trityl radicals versatile ESR spin probes and, in this work, allow OX063 to serve as a stable, chemically adaptable electron-spin sensor embedded in the material under study.

B. Sample and spin environment

We prepare the sample as a 1–10 aL droplet containing OX063 sensor spins dispersed in a 10∶1 trehalose dihydrate:sucrose cryoprotectant mixture. Such trehalose-based matrices are commonly used in structural biology, e.g., for ESR distance measurements, and can preserve molecular structure under low-temperature [46,60,61] and low-hydration conditions [62,63].

Previous measurements show that fluctuating dangling-bond spins on the surface of the silicon nanowire (SiNW) force sensor [Fig. 1(b)] substantially shorten the OX063 electron-spin T_1 via excess relaxation [55]. To mitigate this effect, we mount the droplet at the end of a ∼2–3-μm-long polystyrene spacer attached to the SiNW tip, which separates the sensor spins from fast-relaxing paramagnetic defects on the nanowire. With the spacer in place, we measure T_1 values of 500–700 ms, corresponding to about a tenfold increase over earlier results. Details of the sample attachment are provided in Supplemental Material [64].

To improve experimental throughput, we prepared multiple SiNWs, each with an attached droplet sample, enabling sequential measurements of multiple samples within a single experimental run. The results presented in this work correspond to one such sample, consisting of a ∼1-aL detection volume containing an estimated 140 OX063 molecules. Measurements were performed in high vacuum at a base temperature of 4 K under a static field $B_0 = 0.330$ T aligned with the SiNW axis, corresponding to an electron Larmor frequency of 9.26 GHz. Owing to optical absorption from the interferometric displacement-detection laser, we estimate the SiNW temperature during measurement to be ∼8 K. Further details of the sample preparation are given in Supplemental Material [64].

C. Spin control and mechanical readout

The SQUINT sensing platform, shown in Fig. 1(b), follows the general configuration used in previous nanoMRI experiments [56,57,65]. A SiNW nanomechanical oscillator detects the longitudinal spin magnetization by measuring the force on the electron spins in a magnetic-field gradient. Spin control and detection are performed using a current-focusing field gradient source (CFFGS), which generates both the time-dependent gradients used for mechanical detection and the transverse fields used for spin control. The CFFGS is broadband (dc–10 GHz) and can address both nuclear and electron spins. The silicon chip containing the SiNW array was positioned with piezoactuators so that the selected SiNW was aligned over the center of the CFFGS, with the attached sample approximately 70 nm above the surface.

Driving the CFFGS at the spin Larmor frequency generates the transverse control (Rabi) field $B_1(\mathbf{r}) = \sqrt{B_x^2(\mathbf{r}) + B_y^2(\mathbf{r})}/2$, with $B_x(\mathbf{r}), B_y(\mathbf{r}), B_z(\mathbf{r})$ being the components of the magnetic field at location $\mathbf{r}$. Since the CFFGS field is spatially nonuniform, the resulting electron Rabi frequency $u(\mathbf{r}) = \gamma_e B_1(\mathbf{r})/(2\pi)$ varies across the sample volume, where $\gamma_e/(2\pi) = 28.025$ GHz/T is the electron gyromagnetic ratio. An example of this distribution, measured for the sample used in this work, is shown in Fig. 1(e).

Readout of the sensor spins is conducted by detecting statistical correlations in their spin fluctuations using the modulated alternating gradients generated with currents (MAGGIC) protocol described in our previous work [55–57]. The detected signal is the correlation between the gradient-weighted longitudinal magnetization before and after a control sequence of interest [Fig. 1(d)]. Rather than measuring an average magnetization as in conventional ESR, this correlation measurement detects statistical-spin fluctuations in a maximally mixed ensemble. The signal is proportional to $C \propto \sum_j G^2(\mathbf{r}_j)\mathrm{Tr}[S_j^z(0)S_j^z(\tau_c)]$, where $G(\mathbf{r}_j) = \partial B_z(\mathbf{r}_j)/\partial y$ is the readout gradient at the position of the jth electron, τ_c is the duration of the control sequence, and $S_j^z(t)$ is the Heisenberg-picture z-spin operator.

III. XYXYd SEQUENCE

Preserving the sensor-spin coherence requires a control sequence that averages out both local resonance offsets and electron-electron dipolar interactions, and operates over the broad Rabi frequency distribution generated by the CFFGS [Fig. 1(e)]. For this purpose, we construct a modified XYXY dipolar decoupling sequence based on specifically engineered adiabatic inversions that rescale the dipolar interaction. In the high-field limit, the spin Hamiltonian in the electron rotating frame is $H(t) = H_\Delta + H_D + H_C(t)$, where

$$H_\Delta = -\sum_j \Delta_j S_j^z \tag{1}$$

encompasses all electron spin resonance offsets, including hyperfine interactions to surrounding nuclei,

$$H_D = \sum_{j<k} D_{jk}(3S_j^z S_k^z - \mathbf{S}_j \cdot \mathbf{S}_k) \tag{2}$$

is the secular electron-electron dipolar interaction, and

$$H_C(t) = 2\pi \sum_j u(\mathbf{r}_j)\mathbf{a}(t) \cdot \mathbf{S}_j \tag{3}$$

is the microwave control Hamiltonian. The transverse vector $\mathbf{a}(t)$ satisfies $|\mathbf{a}(t)| \leq 1$ and determines the instantaneous amplitude and phase of the applied field.

Conventional dynamical decoupling sequences based on trains of global π pulses, such as XYXY [66–68], refocus static frequency offsets described by H_Δ but leave the dipolar Hamiltonian H_D unchanged to leading order. For the electron-spin ensemble used here, we measured an inhomogeneous dephasing time of $T_2^* = 78(6)$ ns and a Hahn-echo coherence time of $T_2 = 6(1)$ μs, indicating that suppressing H_Δ alone is insufficient. Achieving the longer coherence times reported in this work therefore requires a sequence that goes beyond conventional spin-echo decoupling by also averaging electron-electron dipolar interactions. This requirement motivates the XYXYd sequence developed here.

To suppress electron-electron dipole interactions, we replace each π pulse by a composite adiabatic inversion consisting of a resonant drive of duration τ_d, sandwiched between two short adiabatic half passages (AHPs) [Fig. 2(a)]. We refer to this composite inversion as the $\hat{\mathbf{n}}$ *primitive*, where $\hat{\mathbf{n}}$ is the constant transverse control axis set by the microwave phase [$\mathbf{a}(t) = \hat{\mathbf{n}}$ during the driven segment].

In the limit of large Rabi frequencies, $2\pi u(\mathbf{r}_j) \gg |D_{jk}|$, the rotating frame unitary describing the central drive segment is

$$U_d(\hat{\mathbf{n}}) \simeq e^{-i2\pi\tau_d \sum_j u(\mathbf{r}_j)\hat{\mathbf{n}}\cdot\mathbf{S}_j} e^{-i\tau_d \bar{H}_d(\hat{\mathbf{n}})}, \tag{4}$$

where

$$\bar{H}_d(\hat{\mathbf{n}}) = -\frac{1}{2}\sum_{j<k} D_{jk}[3(\hat{\mathbf{n}}\cdot\mathbf{S}_j)(\hat{\mathbf{n}}\cdot\mathbf{S}_k) - \mathbf{S}_j\cdot\mathbf{S}_k] \tag{5}$$

is the effective Hamiltonian in the interaction frame of $H_C(t)$, i.e., the toggling frame [69], and τ_d is the drive duration. Hence, for ideal AHPs that are much faster than the timescale of H_D and H_Δ, the $\hat{\mathbf{n}}$-primitive propagator is

$$\begin{aligned} U(\hat{\mathbf{n}}) &= U_{\hat{\mathbf{n}}\to-\hat{\mathbf{z}}} U_d(\hat{\mathbf{n}}) U_{\hat{\mathbf{z}}\to\hat{\mathbf{n}}} \\ &= U_{\hat{\mathbf{z}}\to-\hat{\mathbf{z}}} e^{-i2\pi\tau_d \sum_j u(\mathbf{r}_j)S_j^z} e^{-i\tau_d \bar{H}_d(\hat{\mathbf{z}})}, \end{aligned} \tag{6}$$

where we use the notation $U_{\hat{\mathbf{n}}_1\to\hat{\mathbf{n}}_2}$ to denote a generic unitary that maps the point $\hat{\mathbf{n}}_1$ to $\hat{\mathbf{n}}_2$ on the Bloch sphere. Since $\bar{H}_d(\hat{\mathbf{z}}) = -H_D/2$, an ideal $\hat{\mathbf{n}}$ primitive results in a combination of (1) time-reversed dipolar evolution with half the coupling, (2) a Rabi-frequency-dependent rotation around $\hat{\mathbf{z}}$, and (3) a π rotation. Therefore, for ideal AHPs, an XYXYd sequence [Fig. 2(b)] with free-evolution times $\tau_f = \tau_d/2$ would average out H_D and H_Δ to leading order:

$$[U_0(\tau_f/2)U(\hat{\mathbf{y}})U_0(\tau_f)U(\hat{\mathbf{x}})U_0(\tau_f/2)]^2 \propto \mathbb{1}, \tag{7}$$

with $U_0(\tau) \equiv e^{-i\tau(H_D+H_\Delta)}$ being the free-evolution propagator.

In practice, dipolar evolution during the AHPs is nonnegligible. To quantify the net effect of a control block on an operator h, we numerically evaluate its zeroth-order average Hamiltonian $\bar{h}^{(0)}$ in the toggling frame, and decompose it into components parallel and orthogonal to h with respect to the Hilbert-Schmidt inner product:

$$\Phi_\parallel(h) = \langle h, \bar{h}^{(0)}\rangle / \|h\|^2, \tag{8}$$

$$\Phi_\perp(h) = \|\bar{h}^{(0)} - \Phi_\parallel(h)h\| / \|h\|, \tag{9}$$

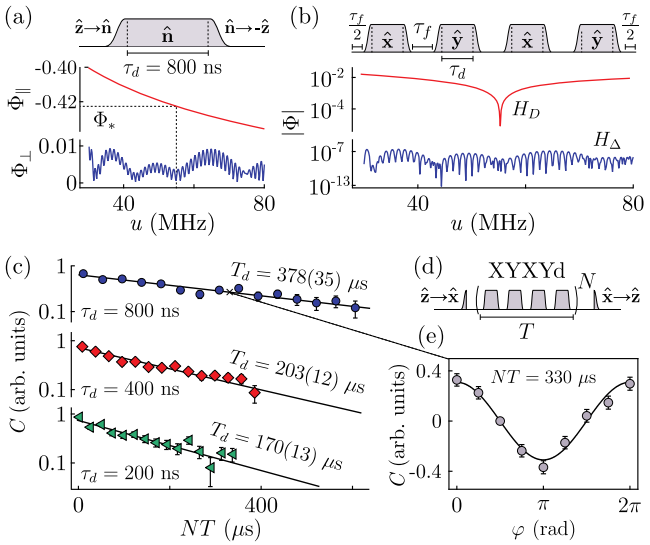


FIG. 2. XYXYd sequence design and simulation. (a) Numerical evaluation of the dipolar rescaling factors $\Phi_\parallel(H_D)$ (red) and $\Phi_\perp(H_D)$ (blue) for a single $\hat{\mathbf{n}}$ primitive with $\tau_d = 800$ ns, showing a rescaling of $\Phi_* = -0.42$ at the center of the Rabi distribution ($u = 55$ MHz). Pulses labeled as $\hat{\mathbf{n}}_1 \to \hat{\mathbf{n}}_2$ denote adiabatic half passages (AHPs) that map $\hat{\mathbf{n}}_1$ to $\hat{\mathbf{n}}_2$ on the Bloch sphere. The AHPs were 67 ns long, and designed using the optimal control protocol given in Ref. [65]. (b) Dipolar $|\Phi(H_D)|$ and resonance offset $|\Phi(H_\Delta)|$ suppression metrics for a single XYXYd block. (c) Measured XYXYd decay curves and associated exponential fits (solid lines) as a function of the total XYXYd time NT. (d) Pulse sequence used in (c), consisting of N repetitions of an XYXYd block of duration T. (e) Phase-accumulation test used to rule out spin locking. An effective z field is introduced by applying a phase shift of $+\varphi/(8N)$ to each $\hat{\mathbf{x}}$ primitive and $-\varphi/(8N)$ to each $\hat{\mathbf{y}}$ primitive. The observed modulation in the signal as a function of φ rules out spin locking during the XYXYd sequence.

TABLE I. Sequence parameters and measured XYXYd decay constants in terms of the total (T_d) and free evolution ($T_{d,\mathrm{free}}$) times.

Sequence parameters			Decay times	
τ_d (ns)	τ_f (ns)	T (μs)	T_d (μs)	$T_{d,\mathrm{free}}$ (μs)
200	95	1.717	170(13)	38(3)
400	192	2.903	203(12)	54(3)
565	278	3.913	151(16)	43(5)
800	395	5.317	378(35)	112(10)
1311	560	7.303	457(48)	140(15)
1600	795	10.117	478(49)	150(15)

where $\Phi_{\parallel}(h)$ quantifies the retained fraction of h, and $\Phi_{\perp}(h)$ measures leakage into orthogonal directions. We use $|\Phi(h)| = \sqrt{\Phi_{\parallel}^2(h) + \Phi_{\perp}^2(h)}$ as a single metric for the suppression of h by the sequence.

For the numerical evaluation of $\bar{h}^{(0)}$, we consider a two-spin system at fixed Rabi frequency u. Figure 2(a) shows $\Phi_{\parallel}(H_D)$ and $\Phi_{\perp}(H_D)$ for a single $\tau_d = 800$-ns $\hat{\mathbf{n}}$ primitive, showing a dipolar rescaling factor of $\Phi_* = -0.42$ at the center of the Rabi distribution, with less than 1% leakage into the orthogonal subspace. Accordingly, choosing $\tau_f = -\Phi_*(\tau_d + 2\tau_{\mathrm{AHP}})$, where $\tau_{\mathrm{AHP}} = 67$ ns is the AHP duration, results in an XYXYd sequence with $|\Phi(H_D)| < 10^{-2}$ across the Rabi distribution [Fig. 2(b)]. Repeating the analysis for the resonance offset term gives $|\Phi(H_\Delta)| \leq 10^{-7}$. Because of the dipolar-averaging condition, τ_d, τ_f, and T are not independent; specifying the total XYXYd block duration T uniquely fixes τ_d and τ_f.

Using this approach, we designed XYXYd sequences of varying drive durations and measured the resulting coherence times. The data for three representative drive durations are shown in Fig. 2(c), with the complete set of extracted time constants provided in Table I. For $\tau_d = 800$ ns, we measured a coherence time of $T_d = 378(35)$ μs. We ruled out spin-locking effects by measuring oscillations generated by an effective z field introduced via controlled phase shifts in the sequence [Fig. 2(e)] [70].

We note that the XYXYd sequence can also be used for Fourier imaging by applying static field gradients during the τ_f intervals, in which case the relevant coherence time, $T_{d,\mathrm{free}}$, is in units of accumulated free evolution time (Table I). For $\tau_d = 800$ ns, we measure $T_{d,\mathrm{free}} = 112(10)$ μs—a factor of 19 longer than the bare T_2.

IV. EXTERNAL-FIELD SENSING

To demonstrate ac magnetic-field sensing with SQUINT, we apply the XYXYd sequence to detect an rf magnetic field generated by the CFFGS. The basic idea is analogous to ac magnetometry protocols used in NV platforms [71]. By timing the XYXYd applications relative to the oscillation of the applied field, each electron spin accrues a coherent phase proportional to the longitudinal component of that field. The evolution under N applications of the XYXYd sequence (denoted XYXYd-N) is governed by the effective Hamiltonian $H_{\mathrm{eff}} = -\sum_j \Omega_N(\mathbf{r}_j, T) S_j^z$, where

$$\Omega_N(\mathbf{r}, T) \equiv \gamma_e \int_{-\infty}^{\infty} d\nu\, \zeta_N(T\nu) \tilde{B}_z(\mathbf{r}, \nu) e^{i\pi N T \nu}, \quad (10)$$

and $\tilde{B}_z(\mathbf{r}, \nu) = \int_{-\infty}^{\infty} dt\, B_z(\mathbf{r}, t) e^{-i2\pi\nu t}$ is the Fourier transform of the longitudinal field $B_z(\mathbf{r}, t)$. The filter function,

$$\zeta_N(T\nu) \equiv \sum_{k=-\infty}^{\infty} \Gamma_k \mathrm{sinc}[NT(\nu - \nu_k)], \quad (11)$$

is the sum over sinc function lobes centered at $\nu_k = 2(2k-1)/T$, with weights Γ_k given by the Fourier components of the toggling-frame S_j^z modulation (see Supplemental Material [64]). These weights determine the sensitivity of the sequence to field components at each harmonic. Here, $\mathrm{sinc}(x) \equiv \sin(\pi x)/(\pi x)$ denotes the normalized sinc function. Hence, the spectral components of B_z that overlap with the filter function result in a measurable modulation of the transverse magnetization, enabling frequency-selective sensing of the applied field.

It is useful to distinguish the response of XYXYd-N from conventional Carr-Purcell or XYXY magnetometry implemented with hard pulses. In the hard-pulse limit, control pulses are treated as instantaneous, and the sensed phase accumulates only during free evolution. This approximation is not valid for XYXYd, where a substantial fraction of each block is spent under microwave drive to average dipolar interactions. We therefore compute the accumulated phase from the full time dependence of the sequence, encoded in the filter function ζ_N in Eq. (10). For an XYXYd-N sequence applied at $t = 0$, an electron spin subject to $B_z(t) = B_{\mathrm{ext}} \cos(2\pi\nu_m t)$ accumulates $\varphi(B_{\mathrm{ext}}) = NT\Omega_N = NT\gamma_e B_{\mathrm{ext}} \cos(\pi N T \nu_m) \zeta_N(T\nu_m)$. At the center of the kth filter-function lobe, this becomes $\varphi(B_{\mathrm{ext}}) = NT\gamma_e B_{\mathrm{ext}} \Gamma_k$.

Operating at a larger index k allows the sequence to detect higher frequencies without reducing the XYXYd block duration T. However, the Fourier weights Γ_k become smaller as k increases, thus reducing the detection sensitivity. In practice, the optimal sensitivity therefore reflects a trade-off between shortening T and operating at a higher k. The calculation of Γ_k, along with the values used in this work, is provided in Sec. VIII of Supplemental Material [64].

Figure 3 summarizes the external-field sensing measurements. By driving the CFFGS at frequency ν_m with peak current I_{pk}, we generated a spatially nonuniform rf field across the sensor ensemble, resulting in each spin accruing the phase $\varphi(B_{\mathrm{ext}})$ according to its local field amplitude. The resulting modulation in the transverse magnetization components can be converted to an observable correlation

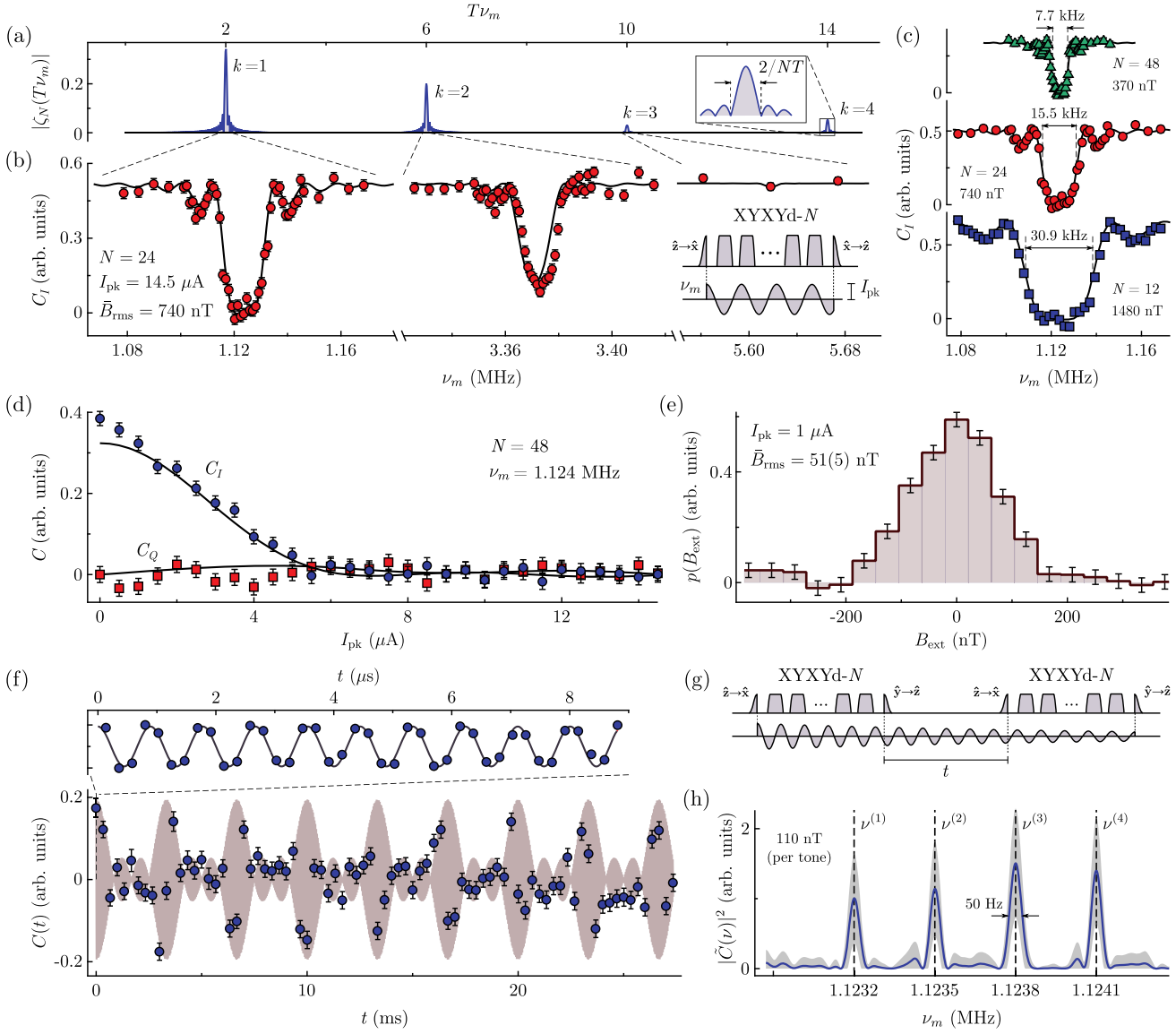


FIG. 3. Quantum sensing of external fields. (a) XYXYd-N filter function magnitude as a function of normalized drive frequency $T\nu_m$, showing the first four filter function lobes. (b) Measured in-phase signal C_I as a function of the drive frequency ν_m for $N = 24$ repetitions of the XYXYd block ($T = 1.780$ μs). The modulation was applied by passing a peak current of $I_{\rm pk} = 14.5$ μA through the CFFGS during the XYXYd sequence (inset). The corresponding ensemble-averaged rms field, inferred from the distribution in (e), was 740(68) nT. (c) Measured in-phase signal for the $k = 1$ lobe at different XYXYd repetitions. The $N \times I_{\rm pk}$ product was kept constant to keep the phase accrued by the electron the same at the center of the lobe. (d) In-phase and quadrature signals measured at the center of the first lobe as a function of the peak CFFGS current $I_{\rm pk}$. The quadrature signal was measured by changing the phase of the last AHP by $\pi/2$. (e) Longitudinal-field distribution $p(B_{\rm ext})$ of the ensemble for 1 μA peak current, extracted from the Fourier transform of the data in (d). The distribution has a full width at half maximum of 210 nT, reflecting the spatial inhomogeneity of the CFFGS field across the detected ensemble. All solid lines in (b)–(d) are calculations using Eq. (12) and the measured $B_{\rm ext}$ distribution (e). (f) Time-domain correlation-spectroscopy signal, (bottom) with and (top) without undersampling. The shaded curve represents the expected modulation $\propto \sum_{n=1}^{4} \cos[2\pi\nu^{(n)}t]$. (g) The correlation spectroscopy pulse sequence. For the measurements in (f), we used $N = 24$. (h) Power spectral density (PSD) of the undersampled data in (f), showing four peaks at the expected frequencies $\nu^{(n)}$ of the applied field. Zero padding was used for visualization of the PSD. All measurements are taken with a $T = 1.780$ μs XYXYd duration. The shaded areas correspond to 68% confidence regions. All reported rms fields have a common relative uncertainty of 9%.

signal using additional AHPs [Fig. 3(b), inset]. The corresponding signal quadratures are

$$\begin{bmatrix} C_I \\ C_Q \end{bmatrix} \propto \int_{-\infty}^{\infty} dB_{\mathrm{ext}} p(B_{\mathrm{ext}}) \begin{bmatrix} \cos\varphi(B_{\mathrm{ext}}) \\ \sin\varphi(B_{\mathrm{ext}}) \end{bmatrix}, \quad (12)$$

where $p(B_{\mathrm{ext}})$ is the readout-gradient-weighted distribution of the z-field amplitude over the sample.

Figures 3(b) and 3(c) show the measured in-phase signal C_I for a $T = 1.780$-μs XYXYd-N sequence, as a function of the drive frequency ν_m for the first three filter function lobes and several values of N. As N increases, the spectral dips narrow, reflecting the narrowing of the filter function lobes, and thus enhanced frequency selectivity. For $N = 48$, we measured a full width at half maximum of 7.7 kHz for the spectral dip. The maximum usable N is ultimately limited by decoherence under XYXYd. For the sequence used here, we measured a coherence time $T_d = 104(5)$ μs, corresponding to 58(3) XYXYd repetitions.

In a separate measurement, we fixed the drive frequency at the center of the first lobe $\nu_m = 2/T = 1.124$ MHz and measured C_I and C_Q as a function of the peak current I_{pk} [Fig. 3(d)] with $\zeta_N(T\nu_m) = \Gamma_1 = 0.34$ and $\varphi(B_{\mathrm{ext}}) = NT\gamma_e\Gamma_1 B_{\mathrm{ext}}$. We introduce the parameter $\kappa \equiv NT\gamma_e\Gamma_1 I_{\mathrm{pk}}/I_{\mathrm{ref}}$, where $I_{\mathrm{ref}} = 1$ μA is a fixed reference current. Writing Eq. (12) in complex form gives $C_I + iC_Q \propto \int dB_{\mathrm{ext}} p(B_{\mathrm{ext}}) e^{i\kappa B_{\mathrm{ext}}}$, such that a Fourier transform over κ yields the distribution $p(B_{\mathrm{ext}})$ associated with the reference current [Fig. 3(e)]. The sample-averaged rms field is $\bar{B}_{\mathrm{rms}} = \int dB_{\mathrm{ext}} |B_{\mathrm{ext}}| p(B_{\mathrm{ext}})/\sqrt{2} = 51(5)$ nT. Modeling the measurements in Figs. 3(b)–3(e) using Eq. (12) and the extracted $p(B_{\mathrm{ext}})$ shows good agreement with the data (solid lines).

The spectral resolution provided by the XYXYd filter function is ultimately limited by the electron coherence time T_d. To enable higher resolution, we employ a correlation spectroscopy sequence [72,73] constructed from two XYXYd-N blocks separated by a free evolution time t, during which the accrued phase from the first block is stored in the longitudinal spin components [Fig. 3(g)]. In the limit where the electron accrues a phase $\ll 1$ during each XYXYd-N block, a measurement of the signal after the second block yields the correlation between the electron phases accrued during the two blocks. The Fourier transform of this signal results in a high-resolution spectrum of the applied field. Theoretical details of the correlation-spectroscopy experiments are provided in Supplemental Material [64].

To demonstrate this method, we applied a four-tone current $I(t) = I_{\mathrm{pk}} \sum_{n=1}^{4} \cos[2\pi\nu^{(n)}t]$ to the CFFGS, with $I_{\mathrm{pk}} = 2.2$ μA per tone and frequencies $\nu^{(n)}$ chosen within the first filter-function lobe, separated by 300 Hz. The drive amplitude for each tone corresponds to a sample-averaged rms z field of 110(10) nT. The resulting time-domain signal is shown in Fig. 3(f). Rather than sampling the oscillations at the Nyquist rate, we undersampled the signal at 3-kHz sampling rate, chosen such that the frequency band of interest [1.12287 MHz, 1.12437 MHz] aliases without overlap into the first Nyquist zone [0, 1.5 kHz], enabling recovery of the spectrum using fewer measurements.

By Fourier transforming the undersampled data, we constructed the power spectral density (PSD) of the four-tone modulation [Fig. 3(h)]. We note that the longest evolution time used in this measurement was ∼30 ms, which is well below the measured electron spin-lattice relaxation time [$T_1 = 671(24)$ ms] and therefore did not approach the T_1-limited maximum time available for correlation measurements. In principle, extending the correlation delay toward the T_1 limit would enable spectral resolutions on the order of a few hertz.

V. NUCLEAR SPIN SENSING AND SPECTROSCOPY

We use the XYXYd sequence to probe the local nuclear spins surrounding each electron-spin sensor molecule. Hyperfine coupling to nearby nuclei produces a narrow band, stochastic magnetic field at the nuclear Larmor frequency that contributes to the longitudinal field experienced by the electron. The sensing principle mirrors the external-field case: by tuning the XYXYd filter function to the Larmor frequency of a given nuclear species, the electron spin accumulates phase from its coupling to those nuclei, resulting in a measurable suppression of the spin echo.

Throughout this section, we model all nuclei as $I = 1/2$ spins and, because XYXYd effectively decouples the electron spins from one another, we analyze the dynamics on a single-electron basis. In the high-field limit, the hyperfine interaction for a given electron spin is $H_{\mathrm{hf}} = \sum_l (A_{0l} I_l^z + \mathbf{A}_{1l} \cdot \mathbf{I}_l) S^z$, where A_{0l} is the secular coupling to the lth nucleus, and the transverse vector $\mathbf{A}_{1l}$ represents the pseudosecular coupling. For an axially symmetric hyperfine tensor, these couplings depend on the angle θ between the tensor's nondegenerate principal axis and the static field. The isotropic-anisotropic decomposition of the hyperfine tensor gives [74]

$$A_0 = A_{\mathrm{iso}} + A_{\mathrm{aniso}}(1 - 3\cos^2\theta), \quad (13)$$

$$A_1 \equiv |\mathbf{A}_1| = \frac{3}{2} A_{\mathrm{aniso}} \sin(2\theta). \quad (14)$$

Under an XYXYd-N sequence, the evolution is described by the effective Hamiltonian $H_{\mathrm{eff}} = \sum_l \zeta_N(T\nu_{\mathrm{nuc}}) A_{1l} I_l^x S^z$ in the interaction frame of the nuclear Zeeman term (Supplemental Material [64]). Here, ν_{nuc} is the nuclear Larmor frequency. For a given realization of the nuclear spin bath, evolution under H_{eff} results in a phase $\varphi = NT \sum_l \zeta_N(T\nu_{\mathrm{nuc}}) A_{1l} I_l^x$ accrued by the electron. As in

the external-field measurements, this phase is converted into a measurable signal by applying AHPs before and after the XYXYd-N sequence, such that the contribution to the signal by each electron is

$$C(t) \propto \langle \cos\varphi \rangle_I = \prod_l \cos\left(\frac{NT\zeta_N(T\nu_{\mathrm{nuc}})A_{1l}}{2}\right), \quad (15)$$

leading to a suppression of the electron spin echo when the filter function is tuned to the nuclear Larmor frequency. Here, $\langle\cdot\rangle_I$ denotes averaging over nuclear spin configurations. The measured signal is the sum of single-electron contributions given by Eq. (15).

Figure 4(b) shows nuclear-spin sensing measurements for different values of N, obtained by sweeping the XYXYd duration T, and hence the location of the filter-function lobes. We observe echo suppression at three values of T, with two arising from different harmonics of the filter function at the ^{1}H Larmor frequency $\nu_{\mathrm{H}} = 14.08$ MHz and a third corresponding to ^{13}C nuclei with $\nu_{\mathrm{C}} = 3.54$ MHz [Figs. 4(a) and 4(b)]. The higher Larmor frequency of ^{1}H necessitated detection at higher harmonics of the filter function, reducing sensitivity. This loss is not intrinsic to the sensing scheme and could be mitigated by operating at a lower static field, thereby lowering ν_{H} and permitting detection with lower filter harmonics.

We further characterized the echo suppression by positioning the XYXYd filter function at a particular Larmor frequency, and varying the number of XYXYd repetitions N. Figures 4(c) and 4(d) show the resulting correlation signal. We independently measured the decay expected from the finite electron coherence time under XYXYd and divided the measured signal by this calibrated decay to remove its contribution. For both spin species, increasing N leads to a progressive suppression of the echo. For the ^{13}C resonance, the emergence of a nonzero plateau at large N indicates that a fraction of OX063 molecules contain an electron spin with negligible coupling to any ^{13}C nuclear spin. The ratio of the initial signal to the large-N plateau yields an estimated fraction of 0.49(2) of OX063 molecules whose electron spin is appreciably coupled to at least one ^{13}C spin. Given the ensemble size, this corresponds to around 70 OX063 molecules contributing to the observed contrast.

To model these measurements, we calculate the expected echo suppression using only the ^{1}H and ^{13}C nuclei on the OX063 molecule, while averaging over molecular orientations and the electron Rabi frequency distribution [Fig. 1(e)]. For ^{1}H nuclei, we use Eq. (15) for the 63 protons on the molecule, with hyperfine couplings computed from Eqs. (13) and (14) using the point-dipole approximation: $A_{\mathrm{iso}} = 0$ and $A_{\mathrm{aniso}} = \mu_0\hbar\gamma_{\mathrm{H}}\gamma_e/(4\pi r^3)$, where $\gamma_{\mathrm{H}}/(2\pi) = 42.6$ MHz/T is the ^{1}H gyromagnetic ratio and r is the nucleus-electron distance. The ^{13}C nuclei require a different treatment because, at natural abundance, each of the 52 carbons has only a 1% probability of being ^{13}C, and several carbon sites lie sufficiently close to the electron that their strong hyperfine couplings fall outside the regime where the effective-Hamiltonian description applies. We therefore model the ^{13}C response using a simulation of the time-dependent Hamiltonian under the applied control waveform, with hyperfine parameters taken from the literature [75,76]. Details of the simulations are provided in Supplemental Material [64].

The simulations [solid lines in Figs. 4(b)–4(d)] reproduce the experimental data, indicating that the signal is dominated by nuclei on the OX063 molecule itself rather than by the surrounding matrix. This conclusion is further supported by the experimentally extracted fraction, 0.49(2), of molecules exhibiting appreciable ^{13}C hyperfine coupling, consistent with the expected ^{13}C occupancy in OX063 at natural abundance.

As in the external-field case, the XYXYd sequence can be extended to correlation spectroscopy using the sequence given in Fig. 4(e). The filter function is positioned at the selected nuclear Larmor frequency. The measured signal $C(t)$ probes the correlation between the electron phases accumulated in the two XYXYd-N blocks, which is modulated by nuclear spin dynamics under secular hyperfine couplings during the correlation delay t. In the small-phase regime, the signal is approximately

$$C(t) \propto \sum_l N^2T^2\Gamma^2A_{1l}^2 \cos\left(\frac{tA_{0l}}{2}\right)\cos(2\pi\nu_{\mathrm{nuc}}t). \quad (16)$$

Here, Γ is the filter function weight. For a derivation of Eq. (16), see Supplemental Material [64].

Figures 4(f) and 4(h) show the resulting time-domain correlation signals for the ^{1}H and ^{13}C resonances, respectively. The corresponding power spectra are shown in Fig. 4(g) and in the inset of Fig. 4(h). Simulations based on the effective Hamiltonian for ^{1}H nuclei and time-dependent waveform simulations for ^{13}C nuclei, using the same modeling assumptions as before, are in good agreement with the measured spectra. The broadening of the local ^{1}H spectrum relative to the independently measured bulk line shape [Fig. 4(g), left inset] directly indicates that the detected nuclei are local to the sensor spins. We note that the sensing protocol is directly compatible with electron- or nuclear-spin decoupling sequences applied during the correlation delay to suppress the hyperfine evolution and thereby narrow the line shape.

We compute the fractional contribution to the correlation signal at $t = 0$ for each nuclear site on the molecule (see Supplemental Material [64] for details). The resulting spatial maps for both nuclei are shown in the insets of Figs. 4(g) and 4(h). The ^{1}H signal is distributed across the molecule with an $A_1^2 \propto 1/r^6$ weighting [Eq. (16)]; in

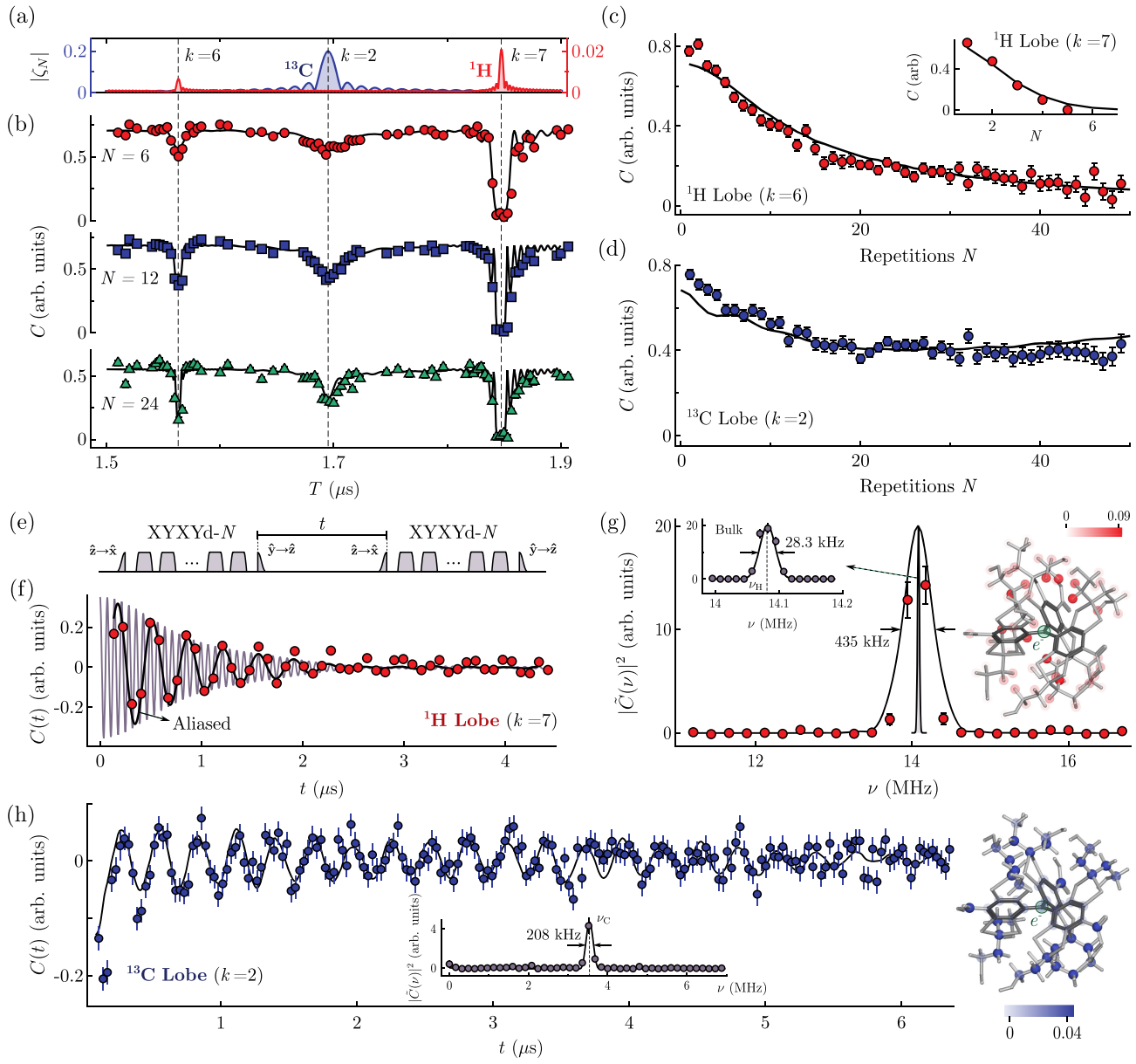


FIG. 4. Nuclear-spin sensing and spectroscopy using the XYXYd sequence. (a) Magnitude of the XYXYd filter function $\zeta_N(T\nu_{\mathrm{nuc}})$ as a function of T, with ν_{nuc} evaluated at the ^{1}H and ^{13}C Larmor frequencies. The two lobes at $T = 1.563$ μs and $T = 1.847$ μs correspond to the $k = 6$, 7 harmonics of the ^{1}H filter function, while the lobe at $T = 1.693$ μs corresponds to the $k = 2$ harmonic for ^{13}C. The separate vertical axes correspond to the ^{1}H (red) and ^{13}C (blue) nuclei. (b) Nuclear-spin sensing measurements obtained by sweeping the XYXYd duration T for different numbers of repetitions N. Echo suppression is observed when a filter-function harmonic is tuned to the ^{1}H or ^{13}C Larmor frequency. Solid lines in all panels denote simulations based on intramolecular ^{1}H and ^{13}C nuclei, unless stated otherwise. (c),(d) Correlation signal measured with the XYXYd filter function placed at the ^{1}H and ^{13}C resonances, respectively, as a function of the number of XYXYd repetitions N. (e) Correlation spectroscopy pulse sequence, consisting of two XYXYd-N blocks separated by a variable free-evolution time t. (f) Time-domain correlation signal measured at the ^{1}H resonance. Similar to the external-field sensing experiments, the data were intentionally undersampled to reduce the number of measurements. (g) Frequency spectrum of the ^{1}H correlation signal reveals a hyperfine-broadened local line shape relative to the independently measured bulk proton NMR spectrum (left-hand inset). The solid curve in the inset depicts a Gaussian fit to the bulk proton line shape. (h) Time-domain correlation signal for the ^{13}C resonance, along with the corresponding frequency spectrum (lower inset). Right-hand insets of (g) and (h): spatial maps of the fractional contribution of each ^{1}H and ^{13}C nucleus on the OX063 molecule to the $t = 0$ correlation signal, respectively. The total signal is normalized to 100%. All quoted spectral widths correspond to full widths at half maximum. Acquisition times for these measurements are provided in Sec. XI of Supplemental Material [64].

particular, 90% of the signal arises from 38 of the 63 hydrogen sites in OX063. For ^{13}C, the 19 sites comprising the central carbon and the three phenyl rings contribute negligibly because their hyperfine couplings are comparable to, or exceed, the electron Rabi frequency; instead, 90% of the signal arises from 26 of the remaining sites. Given the 1% natural abundance, this corresponds to an expected number of about 36 ^{13}C nuclei contributing 90% of the detected signal within the measured sample volume. These measurements demonstrate frequency-selective detection and spectroscopy of a small, local ensemble of nuclear spins using mechanically detected molecular spin sensors.

VI. SENSITIVITY AND OUTLOOK

In this section, we quantify the sensitivity of the SQUINT platform and outline potential improvements for future applications. In all cases considered here, we determine sensitivity by comparing the electron-spin signal produced by the quantity of interest—either an external magnetic field or coupling to a nuclear spin—to the noise expected for a given acquisition time. The signal is set by the phase accumulated by the electron spins under the XYXYd sequence, whereas the noise arises from the thermal-force noise of the mechanical oscillator and fluctuations of the sensor-spin ensemble (spin noise).

For the statistical correlation measurements performed using the MAGGIC spin detection protocol, the signal-to-noise ratio (SNR) has been analyzed in detail in Ref. [55]. A summary of the necessary equations is also provided in Supplemental Material [64]. For a single spin experiencing a local readout gradient G, we define the force-noise equivalent bandwidth $\mathcal{R} \equiv \mu^2 D^2 G^2/(2S_F)$. Physically, $\mathcal{R}$ is the bandwidth in which the oscillator thermal-force noise has integrated variance equal to the force variance of that spin. Larger $\mathcal{R}$ therefore corresponds to improved mechanical readout.

For an ensemble of N_s sensor spins, the standard deviation of a single shot of the correlation measurement may be written in the form $\sigma(N_s\mathcal{R}, \tau_0, \tau_m)$, where $\mathcal{R}$ is interpreted as an ensemble-averaged single-spin bandwidth, obtained by replacing G^2 with its average $\overline{G^2}$. Here, τ_0 is the measure block duration [Fig. 1(d)], μ is the electron magnetic moment, S_F is the (single-sided) thermal-force noise spectral density of the nanomechanical oscillator, and D and τ_m are the duty cycle and spin-correlation time under MAGGIC, respectively [55–57]. Throughout this section, we normalize the expectation value of the total electron signal in the absence of a control sequence to unity, such that $1/\sigma(N_s\mathcal{R}, \tau_0, \tau_m)$ is the single-shot SNR of the bare signal.

For sensing external fields, we consider an XYXYd-N sequence similar to the inset of Fig. 3(b), with the phase of the last AHP shifted by $\pi/2$. For a sinusoidal longitudinal field with amplitude B_{ext} centered at a filter-function lobe with weight Γ, the resulting correlation signal takes the form $\sin(NT\Gamma\gamma_e B_{\text{ext}})e^{-NT/T_d}$. For a fixed total acquisition time τ_{acq}, the SNR is

$$\text{SNR}(B_{\text{ext}}, \tau_0, \tau_m, N) = \sqrt{\frac{\tau_{\text{acq}}}{NT + \tau_0 + \tau_{\text{ovh}}}} \times \frac{\sin(NT\Gamma\gamma_e B_{\text{ext}})e^{-NT/T_d}}{\sigma(N_s\mathcal{R}, \tau_0, \tau_m)}, \quad (17)$$

where $\tau_{\text{ovh}} = 2$ ms accounts for the overhead per shot arising from finite rise and fall times in the MAGGIC protocol [57]. The detection threshold $B_{\text{min}}(N_s\mathcal{R}, \tau_{\text{acq}})$ is defined as the smallest field amplitude for which $\text{SNR}(B_{\text{min}}, \tau_0, \tau_m, N) = 1$, obtained by minimizing B_{min} over experimentally permissible values of τ_0, τ_m, and N at fixed $N_s\mathcal{R}$ and τ_{acq}. The spin-correlation time τ_m can be experimentally reduced by using scrambling pulses to rerandomize the spin ensemble [77]. Accordingly, the optimization over τ_m is restricted to values below the maximum correlation time of 68 ms obtained in our measurements. The details of the optimization are provided in Supplemental Material [64]. Note that unlike sensitivities defined from the local slope of the signal, this definition remains valid in the general nonlinear response regime of the sensor spin to the field.

Figure 5(a) shows a plot of the calculated $B_{\text{min}}(N_s\mathcal{R}, \tau_{\text{acq}})$ detection threshold. The calculation assumes the same XYXYd parameters used in Sec. IV, i.e., $\Gamma = 0.34$ (index $k = 1$), $T = 1.78$ μs, and $T_d = 104$ μs.

For nuclear spin sensing, we consider a model in which each sensor electron is coupled to a single ^{1}H spin at separation vector $\mathbf{r}$. The analysis is analogous to the external-field case. We consider the XYXYd-N correlation spectroscopy sequence shown in Fig. 4(e), evaluated at zero correlation delay ($t = 0$), resulting in a signal of the form $\sin^2(NT\Gamma A_1/2)e^{-2NT/T_d}$ (Supplemental Material [64]). The SNR of the measurement is

$$\text{SNR}(A_1, \tau_0, \tau_m, N) = \sqrt{\frac{\tau_{\text{acq}}}{2NT + \tau_0 + \tau_{\text{ovh}}}} \times \frac{\sin^2(NT\Gamma A_1/2)e^{-2NT/T_d}}{\sigma(N_s\mathcal{R}, \tau_0, \tau_m)}. \quad (18)$$

The nuclear-spin detection threshold $A_{1,\text{min}}(N_s\mathcal{R}, \tau_{\text{acq}})$ is defined as the smallest coupling strength for which $\text{SNR}(A_{1,\text{min}}, \tau_0, \tau_m, N) = 1$, obtained by minimizing $A_{1,\text{min}}$ over experimentally permissible values of τ_0, τ_m, and N at fixed $N_s\mathcal{R}$ and τ_{acq}. Using a point-dipole approximation, we convert $A_{1,\text{min}}$ to a maximum sensor-nucleus separation $r_{\text{max}} = [3\mu_0\hbar\gamma_{\text{H}}\gamma_e/(8\pi A_{1,\text{min}})]^{1/3}$, where we assume optimal orientation of the hyperfine tensor, i.e., $|\sin(2\theta)| = 1$.

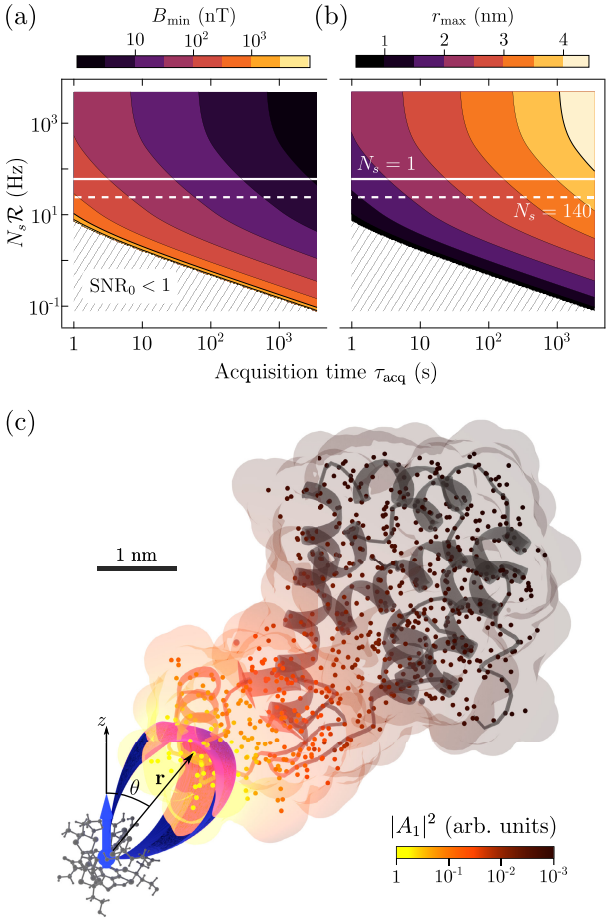


FIG. 5. Magnetic-field and nuclear-spin sensitivity. (a) Calculated minimum detectable longitudinal field amplitude $B_{\min}$ as a function of the ensemble force-noise equivalent bandwidth $N_s\mathcal{R}$ and acquisition time τ_{acq}, in order to achieve unit SNR. (b) Maximum sensor-nucleus separation $r_{\max}$ for unit SNR detection of a single proton spin using the $(t = 0)$ XYXYd correlation spectroscopy sequence. The calculation assumes optimal orientation of the sensor-nucleus separation vector $\mathbf{r}$ relative to the static field. The hatched region in (a) and (b) indicates parameter regimes for which the SNR of the bare electron signal satisfies $\mathrm{SNR}_0 < 1$, making sensing with unit SNR unfeasible. In both panels, the white dashed line at $N_s\mathcal{R} = 25$ Hz indicates the experimental readout parameters for the ~140 sensor-spin ensemble in this work ($\mathcal{R} = 0.18$ Hz per spin), and the solid line indicates the projected parameters achievable with a single sensor spin using near-term improvements to the mechanical readout ($\mathcal{R} = 62$ Hz). (c) Envisioned SQUINT geometry for nuclear-spin sensing in a protein. The schematic shows a lysozyme target with a sensor radical positioned ~1 nm from the protein; ^{13}C nuclei are indicated by dots. The blue surface shows the $|\sin(2\theta)|$ angular dependence of the pseudosecular hyperfine coupling, where θ is the angle between the sensor–nucleus displacement vector $\mathbf{r}$ and the static field. The color map within the protein indicates the relative contribution of each nuclear spin to the zero-delay correlation-spectroscopy signal, $|A_1|^2 \propto \sin^2(2\theta)/r^6$.

Figure 5(b) depicts the calculated $r_{\max}(N_s\mathcal{R}, \tau_{\mathrm{acq}})$ for the same XYXYd parameters used in the external-field case.

The results in Figs. 5(a) and 5(b) illustrate the general dependence of the external-field and nuclear-spin detection thresholds on $N_s\mathcal{R}$ and the acquisition time τ_{acq}. In both cases, larger $N_s\mathcal{R}$ improves the sensitivity and shifts the optimum toward shorter τ_0 and τ_m. Shorter τ_0 reduces the duration of each measurement shot, while shorter τ_m allows more independent statistical-spin configurations to be sampled within the acquisition time. At large $N_s\mathcal{R}$, further improvement is increasingly limited by the minimum accessible τ_0 and the per-shot overhead (Supplemental Material [64]). The hatched regions in Figs. 5(a) and 5(b) indicate $(\tau_{\mathrm{acq}}, N_s\mathcal{R})$ pairs for which the SNR of the bare electron signal is less than unity ($\mathrm{SNR}_0 < 1$), making sensing with unit SNR unfeasible.

The dashed horizontal line in Figs. 5(a) and 5(b) marks $N_s\mathcal{R} = 25$ Hz obtained from the experimental values $\mathcal{R} = 0.18$ Hz and $N_s = 140$ in this work. This corresponds to a mechanical force noise $S_F^{1/2} = 2.4$ aN/$\sqrt{\mathrm{Hz}}$, $(\overline{G^2})^{1/2} = 1.6 \times 10^5$ T/m readout gradient, and $D = 0.98$. With these parameters, a minimum detectable longitudinal field of $B_{\min} = 31$ nT and a maximum sensing distance of $r_{\max} = 2.5$ nm can be achieved with 1 min of averaging using the 140-spin ensemble.

Although we did not optimize the readout parameters in the present measurements, the platform can support substantially larger $\mathcal{R}$ with straightforward improvements. Previous work demonstrated smaller-diameter SiNW arrays with force noise as low as $S_F^{1/2} = 500$ zN/$\sqrt{\mathrm{Hz}}$, achieved through surface passivation and removal of the native oxide by vapor hydrofluoric acid, which reduced laser absorption and enabled operation closer to the 4 K bath temperature [78]. In addition, prior work has realized CFFGS devices that sustain 1.5 times higher current density, which would increase the readout gradient to $\sim 6 \times 10^5$ T/m at 70 nm from the surface [56].

With these improvements, a $D = 1$ duty cycle would result in $\mathcal{R} = 62$ Hz [solid line in Figs. 5(a) and 5(b)]. This would enable detection of a $B_{\min} = 22$ nT external field for $\tau_{\mathrm{acq}} = 1$ min of acquisition using a single sensor spin. In addition, XYXYd correlation spectroscopy would allow detection of a single ^{1}H spin at a maximum separation of $r_{\max} = 2.7$ nm.

Figure 5(c) illustrates an envisioned use of the SQUINT platform, in which a molecular spin sensor is positioned near a protein to probe local nuclear spins using XYXYd correlation spectroscopy. Spatial information could be obtained by Fourier encoding the target nuclei with large, time-dependent magnetic-field gradients applied during the correlation delay. When combined with nuclear-spin decoupling, this approach could enable angstrom-scale

resolution, as demonstrated previously [56]. Multiple sensors could further be used to interrogate distinct regions of the protein, with individual sensors resolved through analogous Fourier encoding. Together, these capabilities would enable spatial mapping of nuclear spins in protein targets.

VII. CONCLUSION

We have presented SQUINT—a nanoscale quantum-sensing framework that combines molecular electron spins, ultrasensitive mechanical spin readout, and high-fidelity dynamical decoupling. Using dipolar decoupling with the XYXYd sequence, we achieve coherence times of ∼400 μs in a nanoscale ensemble of ∼140 electron spins. These capabilities enable frequency-selective sensing of nanotesla-scale rf magnetic fields, as well as detection and spectroscopy of local nuclear-spin ensembles, including ^{1}H and ∼36 naturally abundant ^{13}C spins that dominate the observed signal.

In the present measurements, these nuclear signals originate from nuclei within the OX063 radical itself; however, synthesizing isotopically purified radicals using other isotopes (e.g., ^{12}C, ^{2}H) to suppress the probe's intrinsic nuclear-spin bath [47] would reduce background contributions and extend the same protocol to nuclei in an external target molecule. Notably, the readout parameters demonstrated here support operation with small sensor-spin ensembles, enabling unit-SNR detection of ∼40 electron spins in 1 s of acquisition, corresponding to an OX063 concentration of ∼60 μM for a 1 aL detection volume. With the near-term improvements in mechanical readout quantified in Sec. VI, the platform is projected to reach single-electron sensitivity to nanotesla-scale magnetic fields and to detect individual ^{1}H spins at nanoscale separations.

While the experiments here used SiNW force sensors and trityl-OX063 radicals, the SQUINT platform is not specific to either one. State-of-the-art force transducers such as membrane and string resonators [79–81] can be integrated into the same sensing framework for enhanced force sensitivity. Similarly, the platform is compatible with a broad range of molecular spin systems, including chemically engineered molecular qubits with extended coherence times obtained by tailoring the local nuclear-spin environment [82,83].

A core feature of our approach is the combination of long-lived sensor coherence with large, time-dependent magnetic-field gradients built into the platform. This enables direct integration of the present sensing framework with Fourier-based spatial encoding of either nuclear or electron spins, opening new possibilities for spatially resolved magnetic resonance spectroscopy and imaging on the molecular scale.

The use of molecular systems enables chemical control over sensor placement and environment, without being constrained by the geometry of a host crystal or proximity to a surface. This allows sensor spins to be positioned in close and flexible arrangements relative to a target molecule, with sensing performance optimized through radical choice, functionalization, and engineering of the surrounding matrix. Together, these capabilities establish a versatile and chemically tunable framework for nanoscale quantum sensing, enabling molecular-scale magnetic resonance measurements in complex environments beyond the constraints of defect-based sensors.

ACKNOWLEDGMENTS

This work was undertaken thanks in part to funding from the Canada First Research Excellence Fund (CFREF), and the Natural Sciences and Engineering Research Council of Canada (NSERC). The University of Waterloo's QNFCF facility was used for this work. This infrastructure would not be possible without the significant contributions of CFREF-TQT, CFI, Industry Canada, the Ontario Ministry of Research and Innovation and Mike and Ophelia Lazaridis. Their support is gratefully acknowledged. We would like to thank T. W. Borneman for helpful discussions and D. G. Cory for providing the trityl-OX063 samples, and useful comments.

DATA AVAILABILITY

There are no publicly available research data or software supporting this manuscript. Requests for further information or data should be sent to the authors.

[1] T. Wolf, P. Neumann, K. Nakamura, H. Sumiya, T. Ohshima, J. Isoya, and J. Wrachtrup, *Subpicotesla diamond magnetometry*, Phys. Rev. X **5**, 041001 (2015).

[2] S. Hong, M. S. Grinolds, L. M. Pham, D. L. Sage, L. Luan, R. L. Walsworth, and A. Yacoby, *Nanoscale magnetometry with NV centers in diamond*, MRS Bull. **38**, 155 (2013).

[3] J. F. Barry, J. M. Schloss, E. Bauch, M. J. Turner, C. A. Hart, L. M. Pham, and R. L. Walsworth, *Sensitivity optimization for NV-diamond magnetometry*, Rev. Mod. Phys. **92**, 015004 (2020).

[4] P. Neumann, I. Jakobi, F. Dolde, C. Burk, R. Reuter, G. Waldherr, J. Honert, T. Wolf, A. Brunner, J. H. Shim, D. Suter, H. Sumiya, J. Isoya, and J. Wrachtrup, *High-precision nanoscale temperature sensing using single defects in diamond*, Nano Lett. **13**, 2738 (2013).

[5] G. Kucsko, P. C. Maurer, N. Y. Yao, M. Kubo, H. J. Noh, P. K. Lo, H. Park, and M. D. Lukin, *Nanometre-scale thermometry in a living cell*, Nature (London) **500**, 54 (2013).

[6] D. A. Broadway, B. C. Johnson, M. S. J. Barson, S. E. Lillie, N. Dontschuk, D. J. McCloskey, A. Tsai, T. Teraji, D. A. Simpson, A. Stacey, J. C. McCallum, J. E. Bradby, M. W. Doherty, L. C. L. Hollenberg, and J.-P. Tetienne, *Microscopic imaging of the stress tensor in diamond using in-situ quantum sensors*, Nano Lett. **19**, 4543 (2019).

[7] P. Ovartchaiyapong, K. W. Lee, B. A. Myers, and A. C. B. Jayich, *Dynamic strain-mediated coupling of a single diamond spin to a mechanical resonator*, Nat. Commun. **5**, 4429 (2014).
[8] H. Kono, H. Yukawa, T. Hiromoto, R. Igarashi, Y. Takakusagi, M. Adachi, and Y. Baba, *Quantum life science: A paradigm for life science research*, ACS Nano **20**, 5 (2026).
[9] R. Budakian *et al.*, *Roadmap on nanoscale magnetic resonance imaging*, Nanotechnology **35**, 412001 (2024).
[10] I. Lovchinsky, A. O. Sushkov, E. Urbach, N. P. de Leon, S. Choi, K. D. Greve, R. Evans, R. Gertner, E. Bersin, C. Müller, L. McGuinness, F. Jelezko, R. L. Walsworth, H. Park, and M. D. Lukin, *Nuclear magnetic resonance detection and spectroscopy of single proteins using quantum logic*, Science **351**, 836 (2016).
[11] F. Shi, Q. Zhang, P. Wang, H. Sun, J. Wang, X. Rong, M. Chen, C. Ju, F. Reinhard, H. Chen, J. Wrachtrup, J. Wang, and J. Du, *Single-protein spin resonance spectroscopy under ambient conditions*, Science **347**, 1135 (2015).
[12] A. Ajoy, U. Bissbort, M. D. Lukin, R. L. Walsworth, and P. Cappellaro, *Atomic-scale nuclear spin imaging using quantum-assisted sensors in diamond*, Phys. Rev. X **5**, 011001 (2015).
[13] F. Casola, T. van der Sar, and A. Yacoby, *Probing condensed matter physics with magnetometry based on nitrogen-vacancy centres in diamond*, Nat. Rev. Mater. **3**, 17088 (2018).
[14] B. A. McCullian, A. M. Thabt, B. A. Gray, A. L. Melendez, M. S. Wolf, V. L. Safonov, D. V. Pelekhov, V. P. Bhallamudi, M. R. Page, and P. C. Hammel, *Broadband multi-magnon relaxometry using a quantum spin sensor for high frequency ferromagnetic dynamics sensing*, Nat. Commun. **11**, 5229 (2020).
[15] T. van der Sar, F. Casola, R. Walsworth, and A. Yacoby, *Nanometre-scale probing of spin waves using single electron spins*, Nat. Commun. **6**, 7886 (2015).
[16] D. Khurana, R. H. Jensen, R. Giri, J. Bocquel, U. L. Andersen, K. Berg-Sørensen, and A. Huck, *Sensing of magnetic field effects in radical-pair reactions using a quantum sensor*, Phys. Rev. Res. **6**, 013218 (2024).
[17] A. Finkler and D. Dasari, *Quantum sensing and control of spin-state dynamics in the radical-pair mechanism*, Phys. Rev. Appl. **15**, 034066 (2021).
[18] J. Barton, M. Gulka, J. Tarabek, Y. Mindarava, Z. Wang, J. Schimer, H. Raabova, J. Bednar, M. B. Plenio, F. Jelezko, M. Nesladek, and P. Cigler, *Nanoscale dynamic readout of a chemical redox process using radicals coupled with nitrogen-vacancy centers in nanodiamonds*, ACS Nano **14**, 12938 (2020).
[19] S. Chigusa, M. Hazumi, E. D. Herbschleb, Y. Matsuzaki, N. Mizuochi, and K. Nakayama, *Nuclear spin metrology with nitrogen vacancy center in diamond for axion dark matter detection*, Phys. Rev. D **111**, 075028 (2025).
[20] M. Jiao, M. Guo, X. Rong, Y.-F. Cai, and J. Du, *Experimental constraint on an exotic parity-odd spin- and velocity-dependent interaction with a single electron spin quantum sensor*, Phys. Rev. Lett. **127**, 010501 (2021).
[21] R. Ebadi, M. C. Marshall, D. F. Phillips, J. Cremer, T. Zhou, M. Titze, P. Kehayias, M. S. Ziabari, N. Delegan, S. Rajendran, A. O. Sushkov, F. J. Heremans, E. S. Bielejec, M. V. Holt, and R. L. Walsworth, *Directional detection of dark matter using solid-state quantum sensing*, AVS Quantum Sci. **4**, 044701 (2022).
[22] J. Du, F. Shi, X. Kong, F. Jelezko, and J. Wrachtrup, *Single-molecule scale magnetic resonance spectroscopy using quantum diamond sensors*, Rev. Mod. Phys. **96**, 025001 (2024).
[23] R. Schirhagl, K. Chang, M. Loretz, and C. L. Degen, *Nitrogen-vacancy centers in diamond: Nanoscale sensors for physics and biology*, Annu. Rev. Phys. Chem. **65**, 83 (2014).
[24] J. Zopes, K. S. Cujia, K. Sasaki, J. M. Boss, K. M. Itoh, and C. L. Degen, *Three-dimensional localization spectroscopy of individual nuclear spins with sub-angstrom resolution*, Nat. Commun. **9**, 4678 (2018).
[25] M. H. Abobeih, J. Randall, C. E. Bradley, H. P. Bartling, M. A. Bakker, M. J. Degen, M. Markham, D. J. Twitchen, and T. H. Taminiau, *Atomic-scale imaging of a 27-nuclear-spin cluster using a quantum sensor*, Nature (London) **576**, 411 (2019).
[26] D. Bluvstein, Z. Zhang, and Ania C. Bleszynski Jayich, *Identifying and mitigating charge instabilities in shallow diamond nitrogen-vacancy centers*, Phys. Rev. Lett. **122**, 076101 (2019).
[27] B. K. Ofori-Okai, S. Pezzagna, K. Chang, M. Loretz, R. Schirhagl, Y. Tao, B. A. Moores, K. Groot-Berning, J. Meijer, and C. L. Degen, *Spin properties of very shallow nitrogen vacancy defects in diamond*, Phys. Rev. B **86**, 081406(R) (2012).
[28] T. Rosskopf, A. Dussaux, K. Ohashi, M. Loretz, R. Schirhagl, H. Watanabe, S. Shikata, K. M. Itoh, and C. L. Degen, *Investigation of surface magnetic noise by shallow spins in diamond*, Phys. Rev. Lett. **112**, 147602 (2014).
[29] M. Kim, H. J. Mamin, M. H. Sherwood, K. Ohno, D. D. Awschalom, and D. Rugar, *Decoherence of near-surface nitrogen-vacancy centers due to electric field noise*, Phys. Rev. Lett. **115**, 087602 (2015).
[30] W. K. Lo, Y. Zhang, H. Y. Chow, J. Wu, M. Y. Leung, K. O. Ho, X. Du, Y. Chen, Y. Shen, D. Pan, and S. Yang, *Enhancement of quantum coherence in solid-state qubits via interface engineering*, Nat. Commun. **16**, 5984 (2025).
[31] J. N. Neethirajan, T. Hache, D. Paone, D. Pinto, A. Denisenko, R. Stöhr, P. Udvarhelyi, A. Pershin, A. Gali, J. Wrachtrup, K. Kern, and A. Singha, *Controlled surface modification to revive shallow* NV^- *centers*, Nano Lett. **23**, 2563 (2023).
[32] W. Zheng, K. Bian, X. Chen, Y. Shen, S. Zhang, R. Stöhr, A. Denisenko, J. Wrachtrup, S. Yang, and Y. Jiang, *Coherence enhancement of solid-state qubits by local manipulation of the electron spin bath*, Nat. Phys. **18**, 1317 (2022).
[33] H. Roberts, H. Abudayyeh, X. Li, and X. Li, *Quantum sensing with spin defects beyond diamond*, ACS Nano **19**, 22528 (2025).
[34] J.-P. Tetienne, *Quantum sensors go flat*, Nat. Phys. **17**, 1074 (2021).
[35] R. Rizzato, M. Schalk, S. Mohr, J. C. Hermann, J. P. Leibold, F. Bruckmaier, G. Salvitti, C. Qian, P. Ji, G. V. Astakhov, U. Kentsch, M. Helm, A. V. Stier, J. J. Finley, and D. B. Bucher, *Extending the coherence of spin defects in*

hBN enables advanced qubit control and quantum sensing, Nat. Commun. **14**, 5089 (2023).
[36] C.-J. Yu, S. von Kugelgen, D. W. Laorenza, and D. E. Freedman, *A molecular approach to quantum sensing*, ACS Cent. Sci. **7**, 712 (2021).
[37] C. Bonizzoni, A. Ghirri, F. Santanni, and M. Affronte, *Quantum sensing of magnetic fields with molecular spins*, npj Quantum Inf. **10**, 41 (2024).
[38] H. Singh, N. D'Souza, J. Garrett, A. Singh, B. Blankenship, E. Druga, R. Montis, L. Z. Tan, and A. Ajoy, *High sensitivity pressure and temperature quantum sensing in pentacene-doped P-terphenyl single crystals*, Nat. Commun. **16**, 10530 (2025).
[39] G. Jeschke, *The contribution of modern EPR to structural biology*, Emerging Topics Life Sci. **2**, 9 (2018).
[40] G. Jeschke, *DEER distance measurements on proteins*, Annu. Rev. Phys. Chem. **63**, 419 (2012).
[41] O. Duss, M. Yulikov, G. Jeschke, and F. H.-T. Allain, *EPR-aided approach for solution structure determination of large RNAs or protein–RNA complexes*, Nat. Commun. **5**, 3669 (2014).
[42] P. Roser, M. J. Schmidt, M. Drescher, and D. Summerer, *Site-directed spin labeling of proteins for distance measurements in vitro and in cells*, Org. Biomol. Chem. **14**, 5468 (2016).
[43] J. P. Klare, *Site-directed spin labeling EPR spectroscopy in protein research*, Biol. Chem. **394**, 1281 (2013).
[44] S. Ketter, A. Gopinath, O. Rogozhnikova, D. Trukhin, V. M. Tormyshev, E. G. Bagryanskaya, and B. Joseph, *In situ labeling and distance measurements of membrane proteins in E. coli using Finland and OX063 trityl labels*, Chem. Eur. J. **27**, 2299 (2021).
[45] V. M. Tormyshev, A. S. Chubarov, O. A. Krumkacheva, D. V. Trukhin, O. Y. Rogozhnikova, A. S. Spitsyna, A. A. Kuzhelev, V. V. Koval, M. V. Fedin, T. S. Godovikova, M. K. Bowman, and E. G. Bagryanskaya, *Methanethiosulfonate derivative of OX063 trityl: A promising and efficient reagent for side-directed spin labeling of proteins*, Chem. Eur. J. **26**, 2705 (2020).
[46] M. Malferrari, A. Nalepa, G. Venturoli, F. Francia, W. Lubitz, K. Möbius, and A. Savitsky, *Structural and dynamical characteristics of trehalose and sucrose matrices at different hydration levels as probed by FTIR and high-field EPR*, Phys. Chem. Chem. Phys. **16**, 9831 (2014).
[47] G. Jeschke, N. Wili, Y. Wu, S. Kuzin, H. Karas, H. Hintz, and A. Godt, *Electron-spin decoherence in trityl radicals in the absence and presence of microwave irradiation*, Magn. Reson. **6**, 15 (2025).
[48] A. Savitsky, M. Plato, and K. Möbius, *The temperature dependence of nitroxide spin-label interaction parameters: A high-field EPR study of intramolecular motional contributions*, Appl. Magn. Reson. **37**, 415 (2010).
[49] M. Kveder, D. Merunka, M. Jokić, and B. Rakvin, *Low-temperature electron-spin relaxation in the crystalline and glassy states of solid ethanol*, Phys. Rev. B **77**, 094202 (2008).
[50] H. Chen, A. G. Maryasov, O. Y. Rogozhnikova, D. V. Trukhin, V. M. Tormyshev, and M. K. Bowman, *Electron spin dynamics and spin-lattice relaxation of trityl radicals in frozen solutions*, Phys. Chem. Chem. Phys. **18**, 24954 (2016).
[51] S. L. Bayliss, D. W. Laorenza, P. J. Mintun, B. D. Kovos, D. E. Freedman, and D. D. Awschalom, *Optically addressable molecular spins for quantum information processing*, Science **370**, 1309 (2020).
[52] S. L. Bayliss, P. Deb, D. W. Laorenza, M. Onizhuk, G. Galli, D. E. Freedman, and D. D. Awschalom, *Enhancing spin coherence in optically addressable molecular qubits through host-matrix control*, Phys. Rev. X **12**, 031028 (2022).
[53] A. Mena, S. K. Mann, A. Cowley-Semple, E. Bryan, S. Heutz, D. R. McCamey, M. Attwood, and S. L. Bayliss, *Room-temperature optically detected coherent control of molecular spins*, Phys. Rev. Lett. **133**, 120801 (2024).
[54] J. S. Feder, B. S. Soloway, S. Verma, Z. Z. Geng, S. Wang, B. B. Kifle, E. G. Riendeau, Y. Tsaturyan, L. R. Weiss, M. Xie, J. Huang, A. Esser-Kahn, L. Gagliardi, D. D. Awschalom, and P. C. Maurer, *A fluorescent-protein spin qubit*, Nature (London) **645**, 73 (2025).
[55] S. Tabatabaei, P. Priyadarsi, N. Singh, P. Sahafi, D. Tay, A. Jordan, and R. Budakian, *Large-enhancement nanoscale dynamic nuclear polarization near a silicon nanowire surface*, Sci. Adv. **10**, eado9059 (2024).
[56] H. Haas, S. Tabatabaei, W. Rose, P. Sahafi, M. Piscitelli, A. Jordan, P. Priyadarsi, N. Singh, B. Yager, P. J. Poole, D. Dalacu, and R. Budakian, *Nuclear magnetic resonance diffraction with subangstrom precision*, Proc. Natl. Acad. Sci. U.S.A. **119**, e2209213119 (2022).
[57] W. Rose, H. Haas, A. Q. Chen, N. Jeon, L. J. Lauhon, D. G. Cory, and R. Budakian, *High-resolution nanoscale solid-state nuclear magnetic resonance spectroscopy*, Phys. Rev. X **8**, 011030 (2018).
[58] L. Lumata, Z. Kovacs, A. D. Sherry, C. Malloy, S. Hill, J. van Tol, L. Yu, L. Song, and M. E. Merritt, *Electron spin resonance studies of trityl OX063 at a concentration optimal for DNP*, Phys. Chem. Chem. Phys. **15**, 9800 (2013).
[59] J. R. Brender, S. Kishimoto, G. R. Eaton, S. S. Eaton, Y. Saida, J. Mitchell, and M. C. Krishna, *Trehalose as an alternative to glycerol as a glassing agent for in vivo DNP MRI*, Magn. Reson. Med. **85**, 42 (2021).
[60] V. Meyer, M. A. Swanson, L. J. Clouston, P. J. Boratyński, R. A. Stein, H. S. Mchaourab, A. Rajca, S. S. Eaton, and G. R. Eaton, *Room-temperature distance measurements of immobilized spin-labeled protein by DEER/PELDOR*, Biophys. J. **108**, 1213 (2015).
[61] G. Mathies, S. Jain, M. Reese, and R. G. Griffin, *Pulsed dynamic nuclear polarization with trityl radicals*, J. Phys. Chem. Lett. **7**, 111 (2016).
[62] A. Maiti and S. Daschakraborty, *Unraveling the molecular mechanisms of trehalose-mediated protection and stabilization of Escherichia coli lipid membrane during desiccation*, J. Phys. Chem. B **127**, 4496 (2023).
[63] J. Luyckx and C. Baudouin, *Trehalose: An intriguing disaccharide with potential for medical application in ophthalmology*, Clin. Ophthalmol. **5**, 577 (2011).
[64] See Supplemental Material at http://link.aps.org/supplemental/10.1103/c994-bzx7 for details of sample attachment, derivations, and simulations.

[65] S. Tabatabaei, H. Haas, W. Rose, B. Yager, M. Piscitelli, P. Sahafi, A. Jordan, P. J. Poole, D. Dalacu, and R. Budakian, *Numerical engineering of robust adiabatic operations*, Phys. Rev. Appl. **15**, 044043 (2021).

[66] G. A. Álvarez, A. Ajoy, X. Peng, and D. Suter, *Performance comparison of dynamical decoupling sequences for a qubit in a rapidly fluctuating spin bath*, Phys. Rev. A **82**, 042306 (2010).

[67] M. A. Ali Ahmed, G. A. Álvarez, and D. Suter, *Robustness of dynamical decoupling sequences*, Phys. Rev. A **87**, 042309 (2013).

[68] Z.-H. Wang, G. de Lange, D. Ristè, R. Hanson, and V. V. Dobrovitski, *Comparison of dynamical decoupling protocols for a nitrogen-vacancy center in diamond*, Phys. Rev. B **85**, 155204 (2012).

[69] U. Haeberlen, *High Resolution NMR in Solids Selective Averaging* (Academic Press, New York, 1976).

[70] G. Boutis, P. Cappellaro, H. Cho, C. Ramanathan, and D. Cory, *Pulse error compensating symmetric magic-echo trains*, J. Magn. Reson. **161**, 132 (2003).

[71] J. M. Taylor, P. Cappellaro, L. Childress, L. Jiang, D. Budker, P. R. Hemmer, A. Yacoby, R. Walsworth, and M. D. Lukin, *High-sensitivity diamond magnetometer with nanoscale resolution*, Nat. Phys. **4**, 810 (2008).

[72] Z. Jiang, H. Cai, R. Cernansky, X. Liu, and W. Gao, *Quantum sensing of radio-frequency signal with NV centers in SiC*, Sci. Adv. **9**, eadg2080 (2023).

[73] A. Laraoui, F. Dolde, C. Burk, F. Reinhard, J. Wrachtrup, and C. A. Meriles, *High-resolution correlation spectroscopy of* ^{13}C *spins near a nitrogen-vacancy centre in diamond*, Nat. Commun. **4**, 1651 (2013).

[74] A. Schweiger and G. Jeschke, *Principles of Pulse Electron Paramagnetic Resonance* (Oxford University Press, New York, 2001).

[75] S. Trukhan, V. Yudanov, V. Tormyshev, O. Rogozhnikova, D. Trukhin, M. Bowman, M. Krzyaniak, H. Chen, and O. Martyanov, *Hyperfine interactions of narrow-line trityl radical with solvent molecules*, J. Magn. Reson. **233**, 29 (2013).

[76] M. Bowman, C. Mailer, and H. Halpern, *The solution conformation of triarylmethyl radicals*, J. Magn. Reson. **172**, 254 (2005).

[77] C. L. Degen, M. Poggio, H. J. Mamin, and D. Rugar, *Role of spin noise in the detection of nanoscale ensembles of nuclear spins*, Phys. Rev. Lett. **99**, 250601 (2007).

[78] P. Sahafi, W. Rose, A. Jordan, B. Yager, M. Piscitelli, and R. Budakian, *Ultralow dissipation patterned silicon nanowire arrays for scanning probe microscopy*, Nano Lett. **20**, 218 (2020).

[79] N. Prumbaum, C. L. Degen, and A. Eichler, *From cantilevers to membranes: Advanced scanning protocols for magnetic resonance force microscopy*, Phys. Rev. Appl. **25**, 054048 (2026).

[80] T. Gisler, M. Helal, D. Sabonis, U. Grob, M. Héritier, C. L. Degen, A. H. Ghadimi, and A. Eichler, *Soft-clamped silicon nitride string resonators at millikelvin temperatures*, Phys. Rev. Lett. **129**, 104301 (2022).

[81] C. Reinhardt, T. Müller, A. Bourassa, and J. C. Sankey, *Ultralow-noise SiN trampoline resonators for sensing and optomechanics*, Phys. Rev. X **6**, 021001 (2016).

[82] J. M. Zadrozny, J. Niklas, O. G. Poluektov, and D. E. Freedman, *Millisecond coherence time in a tunable molecular electronic spin qubit*, ACS Cent. Sci. **1**, 488 (2015).

[83] M. Atzori, E. Morra, L. Tesi, A. Albino, M. Chiesa, L. Sorace, and R. Sessoli, *Quantum coherence times enhancement in vanadium(IV)-based potential molecular qubits: The key role of the vanadyl moiety*, J. Am. Chem. Soc. **138**, 11234 (2016).